Academia Open

Vol. 10 No. 2 (2025): December
DOI: 10.21070/acopen.10.2025.13018

ISSN 2714-7444 (online), https://acopen.umsida.ac.id, published by Universitas Muhammadiyah Sidoarjo

Academia Open

Vol. 10 No. 2 (2025): December
DOI: 10.21070/acopen.10.2025.13018

Table Of Contents

Originality Statement

Conflict of Interest Statement

Copyright Statement

Academia Open

Vol. 10 No. 2 (2025): December
DOI: 10.21070/acopen.10.2025.13018

ISSN 2714-7444 (online), https://acopen.umsida.ac.id, published by Universitas Muhammadiyah Sidoarjo

Academia Open

Vol. 10 No. 2 (2025): December
DOI: 10.21070/acopen.10.2025.13018

Article information

Check this article update (crossmark)

Check this article impact (*)

Save this article to Mendeley

(*) Time for indexing process is various, depends on indexing database platform

ISSN 2714-7444 (online), https://acopen.umsida.ac.id, published by Universitas Muhammadiyah Sidoarjo

Academia Open
Vol. 10 No. 2 (2025): December
DOI: 10.21070/acopen.10.2025.13018

Structural and Optical Properties of Fe_2O_3 Nanoparticles for Biosensing Applications

Hiba Fouad Tawfeeq Wali, hibafouad@uowasit.edu.iq, ()
Department of Earth Sciences, College of Science, University of Wasit, Iraq

Saja Abdul Ameer Sayed, ssayed@uowasit.edu.iq, ()
Department of Earth Sciences, College of Science, University of Wasit, Iraq

Ahmed A.Thamer, ahmed.kh@uowasit.edu.iq, ()
Department of physics College of Science, University of Wasit, Iraq

(1) Corresponding author

Abstract

General Background: Nanostructured metal oxides are widely explored for sensing technologies due to their tunable structural and optical behavior. **Specific Background:** Iron oxide (Fe_2O_3), particularly hematite, offers stability, biocompatibility, and catalytic activity suitable for biosensing applications. **Knowledge Gap:** However, the combined structural–optical characterization of Fe_2O_3 synthesized via a simple sol–gel route and its integrated performance within a glucose biosensor remains insufficiently examined. **Aims:** This study investigates the structural, morphological, and optical properties of Fe_2O_3 nanoparticles and evaluates their functionality as an active layer in a glucose oxidase (GOx) sol–gel biosensor. **Results:** XRD confirmed hematite with sharp peaks at ~33.2° and ~35.7°, indicating high crystallinity; UV–Vis/Tauc analysis yielded a direct band gap of 2.1–2.2 eV; SEM/EDS revealed quasi-spherical aggregates composed predominantly of Fe and O. The biosensor exhibited first-order amperometric responses with T90 values of ~26 s (2 mM) and ~34 s (5 mM) and rapid T10 recovery (~2 s). **Novelty:** The combination of sol–gel immobilization and Fe_2O_3's intrinsic catalytic behavior produced fast, stable, and reversibleglucosesensing. **Implications:** These findings support Fe_2O_3–sol–gel platforms as promising candidates for next-generation enzymatic biosensors.

Highlights:

- Fe_2O_3 nanoparticles exhibit high crystallinity and a 2.1–2.2 eV direct band gap.
- Sol–gel Fe_2O_3–GOx biosensor achieves rapid response and recovery times.
- Demonstrates a synergistic catalytic–structural design for reliable glucose detection.

Keywords: Fe_2O_3 Nanoparticles; Hematite; Glucose Biosensor; Optical Properties; Sol–Gel

Introduction

The transition from the macroscopic to the nanoscale is witnessing a radical shift in the scientific landscape, as rapid advances in nanotechnology have contributed to unprecedented clinical achievements . This technology is emerging as a promising tool in biomedical engineering, particularly in the field of loading therapeutic agents, thanks to the unique surface properties of nanoparticles (NPs), which qualify them as effective platforms in drug delivery systems[2-8]. Among these particles, iron oxide is receiving particular attention due to its distinct properties that make it ideal for biomedical applications[9-11]. For example, Fe_2O_3 nanoparticles enhance the stability and permeability of drugs through tissues, prolonging their residence time in the circulation . These particles also enable more effective treatment with lower drug doses, thanks to their ability to control drug release, reducing toxicity and limiting drug accumulation in healthy tissue .These advantages, coupled with the biocompatibility of iron oxide nanoparticles, have attracted extensive research interest in recent decades. The properties of these particles are influenced by multiple factors, such as shape, crystalline structure, size, and preparation method. Surface modifications, resulting from their large specific surface area and high porosity, also enable their use as pH sensors in drug delivery systems .Iron oxide nanoparticles are of additional interest due to their magnetic properties, which allow them to be guided by external magnetic fields to target specific sites in the body, enhancing drug delivery to tumors, for example . These particles also possess electrical catalytic capabilities that accelerate the response in redox-sensitive drug delivery systems .In the context of tissue engineering, nanoparticles are used as replacements for damaged tissue due to their ability to mimic the extracellular matrix, supported by a high surface-to- volume ratio that enhances the efficiency of drug loading and gradual release [18-20]. The diverse physicochemical properties of Fe_2O_3 are also exploited to stimulate cell proliferation and tissue regeneration, particularly in applications such as bone engineering.To ensure the effectiveness of scaffolds in tissue engineering, they must have sufficient porosity to support nutrient and gas transport, which can be achieved using iron oxide nanoparticles . Particles smaller than 10 nm also exhibit superior magnetic properties and immune cell evasion, with excellent drug retention and high electrical conductivity, enhancing their biological applications[25-27] .

A glucose biosensor couples a selective biorecognition step—typically the glucose oxidase (GOx) reaction—with an electrochemical transducer that quantifies either O_2 consumption or the H_2O_2 generated when GOx oxidizes β-D-glucose to D-glucono-δ-lactone, enabling rapid, sensitive, point-of-care measurements .

In our design, iron oxide prepared by the sol–gel route serves as the active sensing layer and enzyme host: sol–gel matrices provide controlled porosity and high purity that stabilize GOx immobilization and facilitate mass transport at the electrode–electrolyte interface.

Beyond acting as a scaffold, Fe_3O_4 exhibits intrinsic peroxidase-like “nanozyme” activity that accelerates H_2O_2 redox, improving signal gain; this catalytic behavior is well established and has been leveraged in Fe_3O_4-based glucose electrodes with low detection limits and good stability[30-32].

Clinically, enzymatic strips based on GOx remain the mainstay, while designs using GDH-PQQ require care because certain nonglucose sugars (e.g., maltose) can cause falsely elevated readings—an interference documented by regulators and clinical studies.

Method

A. Experimental and Materials Preparation

1. **Preparation of Iron oxide (Fe_2O_3)**

We weigh (4) grams of iron and place it in a glass beaker containing (50) ml of distilled water and place the mixture on the magnetic stirrer to obtain a homogeneous mixture. After the iron dissolves completely in the water, we add drops of sodium hydroxide (NaoH) and the drops are added continuously until it turns into a gel and we measure its acidity (PH) and it is about (9). We put the mixture in a tube, then put it in the centrifuge for (10) minutes, the device separates the substance from the solvent, as the substance collects at the bottom while the liquid remains at the top. Then we get rid of the liquid and throw it away. We add distilled water to the remaining substance at the bottom of the tube, and mix it well until the substance is homogeneous with the distilled water, and we put it in the device again, which is, we repeat the process twice. After separating the substance from the liquid, we get rid of the liquid, that is, we throw it away, so the substance remains in the tube. We pour it into a mold and place it in a convection oven at a temperature of (100°C) to dry. After the material dries, it becomes a powder. We grind it with a hand mortar to obtain a fine powder, and then put it in the oven again at a temperature of (550C°) degrees Celsius for two hours. After completing the process, we obtain iron oxide (Fe_2O_3).

Results and Discussion

A. XRD Analysis

X-ray diffraction (XRD) pattern of a sample of iron oxide, specifically (Fe_2O_3), as shown in Fig 1. The XRD pattern shows characteristic diffraction peaks of (Fe_2O_3). The main peaks are two peaks of maximum intensity at 33.24° (210) and 35.72° (10-1). Minor peaks are located at approximately 24.12° (110), 29.52° (202), 54.04° (312), 75° 44s (433), 62.44° (310), and 62.48° (2-1-1). Crystallinity Evaluation The sharp, well-defined peaks indicate that the sample is well crystalline. The background shows a minimally amorphous character, indicating a highly crystalline material. Phase Purity The diffraction pattern matches the standard pattern of Fe2O3. Large, unindexed peaks appear, indicating relatively high phase purity. The peak positions are in good agreement with the JCPDS standard card (96-101-1241) for hematite. Crystal size analysis: The relatively narrow peak lengths indicate well-developed crystallinity of the main peaks, and XRD analysis confirms the successful synthesis of (Fe2O3) as the dominant iron oxide phase. The well-defined peaks and good crystallization density indicate a well-crystalline sample with minimal impurities or amorphous content.

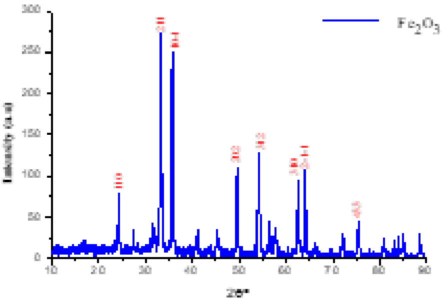

Figure 1: XRD spectra of Fe_2O_3 sample

Table1. Fabrication and Characterization of Fe_2O_3 Blends Nanoparticles.

2θ (Deg.)	FWHM	Crystallite size (nm)	Average Crystallite size (nm)
24.19	0.30	27.47	28.15
33.21	0.34	24.67	
35.68	0.25	34.03	
49.54	0.32	27.07	
54.15	0.37	24.05	
62.52	0.34	27.01	
64.08	0.30	31.76	
75.44	0.34	29.13	

B. The Morphological Investigations

Scanning Electron Microscope (SEM) image analysis of the Fe2O3 sample SEM images at different magnifications 200 nm, and 500 nm for the iron oxide sample show several important morphological properties that can be analyzed as These micrographs show a hierarchical structure of iron oxide particles with several notable features Particle morphology The primary structure consists of quasi-spherical or ovoid nanoparticles These particles show significant aggregation, forming larger secondary structures The edges of individual particles appear somewhat rounded rather than faceted These primary particles form aggregates ranging in diameter from submicron's to several microns The size distribution is relatively polydisperse, indicating possible differences in nuclear composition and growth during synthesis The particles show a strong tendency towards agglomeration, forming cluster-like aggregates Some regions show denser arrangements while other regions show more porous aggregates.

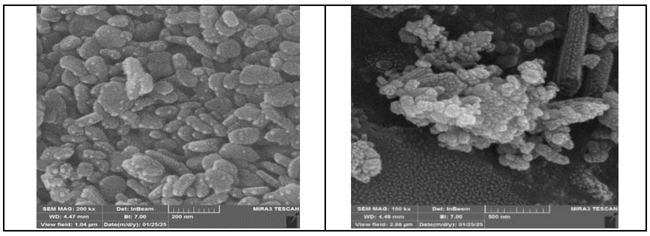

Figure 2: SEM image of Fe_2O_3 with different magnification

This a single-element Figure 3- showing the potassium-alpha emission of iron across the sample surface. The bright green spots indicate the presence and distribution of iron atoms. The distribution of iron appears relatively homogeneous but with some variations in concentration. Areas with dense clusters of green dots represent a higher concentration of iron. Some darker areas indicate areas with lower iron content. The overall coverage suggests that iron is the major component, consistent with the EDX spectrum. Fig3-b: Multi-element mapping. Elemental composite showing the spatial distribution of multiple elements on the sample surface. O (oxygen) is likely red. Zinc (Zn) is likely cyan. Fe (iron) is likely green. Cl (chlorine) is likely blue. Na (sodium) appears to be present, probably pink. Sample structure: The heterogeneous distribution suggests that this may be a mixture of different compounds (iron oxides, zinc compounds, chlorides).

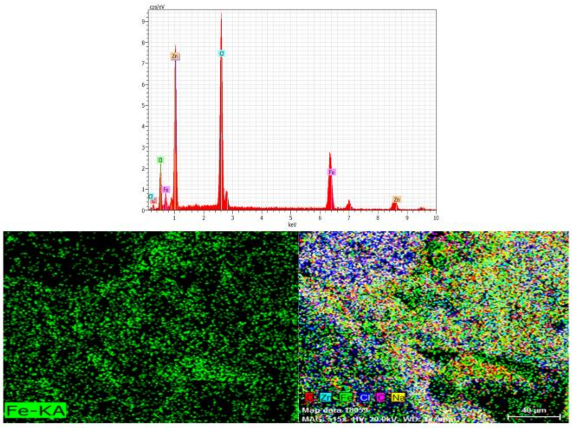

Figure 3: EDS /mapping images of Fe_2O_3

Table 2: Summarizes the map sum spectrum of the sample Fe_2O_3

Eiment	Linetype K-series	[wt.%]	[wt.%]
C	6	7.53	8.74
O	8	17.77	20.62
Na	11	13.62	15.8
Cl	17	20.37	23.64
Fe	26	17.6	20.42
Zn	30	9.3	10.79
Total:	86.19	100	100

C. The Optical Studies

This spectrum shows the relationship of absorbance to the wavelength of light in Figure 5-a. We can obtain the absorption spectrum from about 200 nm to 800 nm, covering the entire ultraviolet and visible region. The optical spectrum appears strongly in the ultraviolet region and along the visible optical wavelengths. The absorption decreases with the increase in the wavelength, especially after 550 nm Also, the characteristic electronic transitions appear. Strong absorption appears in the 200-400 nm region. As a result, transfers occur from the O^{2-} (2p) orbitals to the Fe^{3+} (3d) orbitals. A broad peak is measured in the 400-550 nm region, due to the natural absorption in the 550-600 nm region. This represents the minimum flame required for electron traces from the sharing band to their bonding band. This location is responsible for the characteristic red-brown color of hematite. Figure 5-b shows the index between $(\alpha h\nu)^2$ on the vertical axis and the photon energy ($h\nu$) on the horizontal axis, where α is the absorption coefficient, h is an empty constant, and ν is the frequency of light. The use of the exponent 2 in $(\alpha h\nu)^2$ indicates the training in direct electronic transactions. Legitimate (direct transition allowed). Obtaining an energy of 2.1 to 2.2 eV. This value is assigned to all with the reference standard values for hematite-Fe_2O_3 (2.0-2.2 eV). Electronic transition properties: The clear linear part in 5-b (Figure) is part of the direct electron transition type. The overall growth indicates the crystal structure of the sample. The tendency towards the linear part reflects the quality of the crystals and the lack of crystal defects. The optical absorption properties and the clarity value clearly confirm that the sample is pure hematite Fe_2O_3

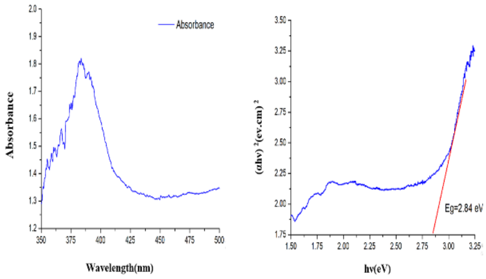

A B

Figure 4: (A) the optical absorbance spectra against the wavelength of the as-prepared sample (Fe_2O_3), (B) Band gap energy curve of prepared (Fe_2O_3).

D. Biosensor application

Figure (6) and Table (3) show responses at 2 mM and 5 mM glucose that show the expected first-order rise for an enzymatic (GOx-based) amperometric sensor that transduces the H_2O_2 generated by glucose oxidation; by the IUPAC convention, the measured T90 values of 26 s (2 mM) and 34 s (5 mM) denote the time to reach 90% of the new steady state after each concentration step, while the T10 recovery values of ≈ 2 s indicate the time to decay to 10% of the preceding plateau after switching back to PBS [34].

The slightly slower T90 at the higher concentration is consistent with known kinetic/mass-transport constraints in first-generation GOx sensors—specifically, local oxygen deficit at elevated glucose and product-accumulation effects—which can slow the approach to steady state despite the larger driving force[35, 36].

The short, concentration-independent ~2 s recovery reflects efficient wash-out and minimal fouling within the sol–gel host, whose controlled porosity facilitates rapid diffusion of glucose and H_2O_2 to and from the enzyme layer[37, 38]. the iron-oxide phase (magnetite) possesses peroxidase-like nanozyme activity, which can accelerate H_2O_2 turnover and help both the rise and the clearance of the signal, contributing to fast, reversible transients[31, 39]. the 26–34 s response paired with ~2 s recovery is within the performance envelope reported for GOx glucose electrodes and indicates a well-coupled reaction–diffusion system in the sol–gel/iron-oxide architecture[40]

.

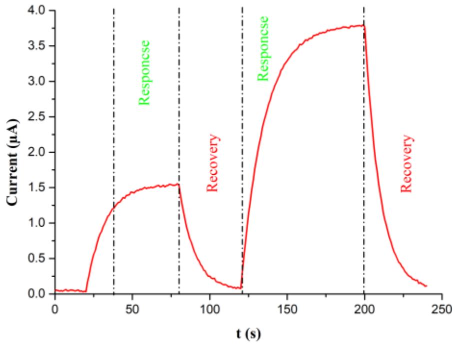

Figure 5:Current–time response and recovery of the glucose biosensor at different concentrations

Table 3: Response (T_{90}) and recovery (T_{10}) times of the biosensor for 2 mM and 5 mM glucose.

Step	Time	Value
2 mM	T90(s)	26
2mM	T 10(s)	2
5 mM	T 90(s)	34
5 mM	T 10	2

Conclusions

The iron oxide (Fe_2O_3) expected structural (hematite) and optical (2.1–2.2 eV) signatures and, when embedded in a sol–gel host with GOx, enabled rapid, reversible amperometric glucose sensing (T90 ≈ 26–34 s; T10 ≈ 2 s). The short recovery and robust step responses point to a well-coupled reaction–diffusion process within the porous sol–gel/Fe-oxide layer and are consistent with state-of-the-art enzymatic glucose devices. Looking forward, work should quantify calibration performance (sensitivity, linear range, LOD/LOQ), interferences (ascorbate, urate, fructose), oxygen-dependence mitigation, and long-term stability, while leveraging Fe-oxide's established peroxidase-like activity to enhance H_2O_2 electrocatalysis.

Acknowledgments

The authors gratefully acknowledge the Postgraduate Laboratories and the Materials Laboratory at the College of Science, University of Wasit (Iraq), for access to instrumentation and steady technical support throughout this work. We thank the laboratory staff for their assistance with sample preparation, instrument calibration, and safety procedures, and the College of Science administration for facilitating scheduling and maintenance of the facilities

References

[1] M. Z. Iqbal and A. Wu, "Magnetic Nanohybrids for Magnetic Resonance Imaging and Phototherapy Applications," in *Tissue Engineering and Nanotheranostics*. World Scientific, 2018, pp. 101–149.

[2] M. Pourmadadi *et al.*, "The Synthesis and Characterization of Double Nanoemulsion for Targeted Co-Delivery of 5-Fluorouracil and Curcumin Using pH-Sensitive Agarose/Chitosan Nanocarrier," *Journal of Drug Delivery Science and Technology*, vol. 70, p. 102849, 2022.

[3] F. Brero *et al.*, "Hadron Therapy, Magnetic Nanoparticles and Hyperthermia: A Promising Combined Tool for Pancreatic Cancer Treatment," *Nanomaterials*, vol. 10, no. 10, p. 1919, 2020.

[4] L. P. Ferreira *et al.*, “Assisted Synthesis of Coated Iron Oxide Nanoparticles for Magnetic Hyperthermia,” *Nanomaterials*, vol. 12, no. 11, p. 1870, 2022.

[5] M. Pourmadadi *et al.*, “Porous Alumina as Potential Nanostructures for Drug Delivery Applications: Synthesis and Characteristics,” *Journal of Drug Delivery Science and Technology*, vol. 77, p. 103877, 2022.

[6] A. Samadi *et al.*, “Curcumin-Loaded Chitosan-Agarose-Montmorillonite Hydrogel Nanocomposite for the Treatment of Breast Cancer,” in *Proc. 27th National and 5th International Iranian Conference on Biomedical Engineering (ICBME)*. IEEE, 2020, pp. 148–153.

[7] Z. Mirzaie, M. Barati, and M. A. Tokmedash, “Anticancer Drug Delivery Systems Based on Curcumin Nanostructures: A Review,” *Pharmaceutical Chemistry Journal*, vol. 54, no. 4, pp. 353–360, 2020.

[8] M. A. Tokmedash *et al.*, “Synthesis of Smart Carriers Based on Tryptophan-Functionalized Magnetic Nanoparticles for 5-Fluorouracil Delivery,” *Biomedical Materials*, vol. 17, no. 4, p. 045026, 2022.

[9] A. M. Davarpanah *et al.*, “(1-x) BaFe12O19/xCoFe2O4 Hard/Soft Magnetic Nanocomposites: Synthesis, Physical Characterization, and Antibacterial Activities,” *Journal of Molecular Structure*, vol. 1175, pp. 445–449, 2019.

[10] S. M. Taimoory *et al.*, “Synthesis and Characterization of a Magnetite Nanoparticle with Potent Antibacterial Activity and Low Mammalian Toxicity,” *Journal of Molecular Liquids*, vol. 265, pp. 96–104, 2018.

[11] M. N. Hajbaba *et al.*, “The Function of Chitosan/Agarose Biopolymer on Fe2O3 Nanoparticles and Their Effects on MCF-7 Cells and BCL2/BAX Expression,” *Biotechnology Progress*, vol. 39, no. 1, p. e3305, 2023.

[12] M. Pourmadadi *et al.*, “Theranostic Applications of Stimulus-Responsive Systems Based on Fe2O3,” *Pharmaceutical Nanotechnology*, vol. 10, no. 2, pp. 90–112, 2022.

[13] Z. Qiao and X. Shi, “Dendrimer-Based Molecular Imaging Contrast Agents,” *Progress in Polymer Science*, vol. 44, pp. 1–27, 2015.

[14] A. Rahdar *et al.*, “Iron Oxide Nanoparticles: Synthesis, Physical Characterization, and Intraperitoneal Biochemical Studies in *Rattus norvegicus*,” *Journal of Molecular Structure*, vol. 1173, pp. 240–245, 2018.

[15] R. Xing, H. Lin, P. Jiang, and F. Qu, “Biofunctional Mesoporous Silica Nanoparticles for Magnetically Oriented Targeting and pH-Responsive Ibuprofen Release,” *Colloids and Surfaces A*, vol. 403, pp. 7–14, 2012.

[16] Y. Ye *et al.*, “Corrosion Protective Mechanism of Smart Graphene-Based Self-Healing Coating on Carbon Steel,” *Corrosion Science*, vol. 174, p. 108825, 2020.

[17] S. E. Korkut *et al.*, “TEMPO-Functionalized Zinc Phthalocyanine: Synthesis, Magnetic Properties, and Electrochemical Sensing of Ascorbic Acid,” *Dalton Transactions*, vol. 45, no. 7, pp. 3086–3092, 2016.

[18] A. Hasan *et al.*, “Nanoparticles in Tissue Engineering: Applications, Challenges and Prospects,” *International Journal of Nanomedicine*, pp. 5637–5655, 2018.

[19] Y. Xu *et al.*, “pH and Redox Dual-Responsive MSN-SS-CS for Drug Delivery in Cancer Therapy,” *Materials*, vol. 13, no. 6, p. 1279, 2020.

[20] M. Pourmadadi *et al.*, “UiO-66 Metal-Organic Framework Nanoparticles for Biomedical Applications: A Comprehensive Review,” *Journal of Drug Delivery Science and Technology*, vol. 76, p. 103758, 2022.

[21] R. Eivazzadeh-Keihan *et al.*, “Metal-Based Nanoparticles for Bone Tissue Engineering,” *Journal of Tissue Engineering and Regenerative Medicine*, vol. 14, no. 12, pp. 1687–1714, 2020.

[22] K. Kim and J. P. Fisher, “Nanoparticle Technology in Bone Tissue Engineering,” *Journal of Drug Targeting*, vol. 15, no. 4, pp. 241–252, 2007.

[23] S. Zhang, S. Vijayavenkataraman, W. F. Lu, and J. Y. Fuh, “Computational Methods for Designing Tissue Engineering Scaffolds,” *Journal of Biomedical Materials Research B*, vol. 107, no. 5, pp. 1329–1351, 2019.

[24] A. Eltom, G. Zhong, and A. Muhammad, “Scaffold Techniques and Designs in Tissue Engineering,” *Advances in Materials Science and Engineering*, vol. 2019, p. 3429527, 2019.

[25] M. Tadic *et al.*, “Rhombohedron and Plate-Like Hematite (α-Fe2O3) Nanoparticles: Synthesis, Structure, Morphology, and Magnetic Properties,” *Materials Research Bulletin*, vol. 133, p. 111055, 2021.

[26] P. Dash *et al.*, “Biomedical Properties of Ferromagnetic α-Fe2O3 Nanoparticles,” *Ceramics International*, vol. 46, no. 16, pp. 26190–26204, 2020.

[27] M. Shahrousvand *et al.*, “Flexible Magnetic Polyurethane/Fe2O3 Nanocomposites for Biomedical Applications,” *Materials Science and Engineering C*, vol. 74, pp. 556–567, 2017.

[28] E. H. Yoo and S. Y. Lee, “Glucose Biosensors: An Overview of Use in Clinical Practice,” *Sensors*, vol. 10, no. 5, pp. 4558–4576, 2010.

[29] U. Narang *et al.*, “Glucose Biosensor Based on a Sol–Gel-Derived Platform,” *Analytical Chemistry*, vol. 66, no. 19, pp. 3139–3144, 1994.

[30] O. S. Wolfbeis *et al.*, “Sol–Gel-Based Glucose Biosensors Employing Optical Oxygen Transducers,” *Biosensors and Bioelectronics*, vol. 15, no. 1, pp. 69–76, 2000.

[31] L. Gao *et al.*, “Intrinsic Peroxidase-Like Activity of Ferromagnetic Nanoparticles,” *Nature Nanotechnology*, vol. 2, no. 9, pp. 577–583, 2007.

[32] Y. Huang, J. Ren, and X. Qu, “Nanozymes: Classification, Catalytic Mechanisms, and Applications,” *Chemical Reviews*, vol. 119, no. 6, pp. 4357–4412, 2019.

[33] J. P. Frias *et al.*, “Adverse Events from False Glucose Readings Using GDH-PQQ Strips,” *Diabetes Care*, vol. 33, no. 4, pp. 728–729, 2010.

[34] International Union of Pure and Applied Chemistry, “Response Time,” in *Compendium of Analytical Nomenclature*, 4th ed. IUPAC, 2023.

[35] S. A. Pullano *et al.*, “Glucose Biosensors in Clinical Practice: Principles and Perspectives,” *Theranostics*, vol. 12, no. 2, pp. 493–511, 2022.

[36] Z. Zhu *et al.*, “A Critical Review of Glucose Biosensors Based on Carbon Nanomaterials,” *Sensors*, vol. 12, no. 5, pp. 5996–6022, 2012.

[37] J. A. Ortega-Contreras *et al.*, “Glucose Sensor Using Sol–Gel Layer on PMMA Optical Fiber,” *Gels*, vol. 9, no. 8, 2023.

[38] L. Qingwen *et al.*, “Immobilization of Glucose Oxidase in Sol–Gel Matrix for Chemiluminescent Sensor,” *Materials Science and Engineering C*, vol. 11, no. 1, pp. 67–70, 2000.

[39] H. Dong *et al.*, “Depletable Peroxidase-Like Activity of Fe3O4 Nanozymes,” *Nature Communications*, vol. 13, p. 5365, 2022.

[40] J. Wang, “Electrochemical Glucose Biosensors,” *Chemical Reviews*, vol. 108, no. 2, pp. 814–825, 2008. 825.